

Article

The Effect of Mn Substitution on Natural Sphalerites by Means of Raman Spectroscopy: A Case Study of the Săcărâmb Au–Ag–Te Ore Deposit, Apuseni Mountains, Romania

George Dincă ^{1,2} , Andrei Ionuț Apopei ^{3,*} , Robert Szabo ¹ and Andreea Elena Maftei ⁴

¹ GeoEcolab Laboratory, Geological Institute of Romania, Str. Caransebeș Nr. 1, 012271 Bucharest, Romania; georgedinca@rocketmail.com (G.D.); robert21szabo@gmail.com (R.S.)

² Research Center for Ecological Services (CESEC), University of Bucharest, 050663 Bucharest, Romania

³ Department of Geology, Faculty of Geography and Geology, “Alexandru Ioan Cuza” University of Iași, 700505 Iași, Romania

⁴ Institute for Interdisciplinary Research, Department of Exact and Natural Sciences, “Alexandru Ioan Cuza” University of Iași, Alexandru Lăpușneanu Str., No. 26, 700057 Iași, Romania; andreea.maftei@uaic.ro

* Correspondence: andrei.apopei@uaic.ro

Abstract: Natural samples of sphalerites containing Mn in the range $0 \leq x \leq 0.25$ apfu from the Săcărâmb Au–Ag–Te ore deposit, found in the Apuseni Mountains, Romania, were investigated using Raman spectroscopy to determine its capability to provide estimates of Mn content. Raman data for the natural Mn-rich sphalerite have not been published so far, with the largest concentration of Mn in sphalerites being from Romanian territory (i.e., 14.1 wt.%). The results are in good agreement with SEM-EDS data. In this study, three genetic types of sphalerites were identified: from ferroan $(Zn_{0.87}Fe_{0.16})_{\Sigma=1.03}S_{0.97}$ to manganoferroan $(Zn_{0.77}Mn_{0.14}Fe_{0.06})_{\Sigma=0.97}S_{1.03}$, as well as mangan-rich $(Zn_{0.8}Mn_{0.25})_{\Sigma=1.05}S_{0.95}$ compositions. Sphalerites with a high content of Mn (up to 14.1 wt.%) were strongly connected to the presence of alabandite in the mineralized assemblages. The formation of several types of sphalerites in the Săcărâmb Au–Ag–Te ore deposit was caused by the succession of different types of hydrothermal fluids and the interaction between the fluids and the host materials (host rocks and earlier mineralized stages).

Keywords: manganian sphalerite; alabandite; hydrothermal; Raman spectroscopy; Apuseni Mountains



Citation: Dincă, G.; Apopei, A.I.; Szabo, R.; Maftei, A.E. The Effect of Mn Substitution on Natural Sphalerites by Means of Raman Spectroscopy: A Case Study of the Săcărâmb Au–Ag–Te Ore Deposit, Apuseni Mountains, Romania. *Minerals* **2022**, *12*, 885. <https://doi.org/10.3390/min12070885>

Academic Editor: Panagiotis Voudouris

Received: 3 June 2022

Accepted: 13 July 2022

Published: 14 July 2022

Publisher’s Note: MDPI stays neutral with regard to jurisdictional claims in published maps and institutional affiliations.



Copyright: © 2022 by the authors. Licensee MDPI, Basel, Switzerland. This article is an open access article distributed under the terms and conditions of the Creative Commons Attribution (CC BY) license (<https://creativecommons.org/licenses/by/4.0/>).

1. Introduction

Sphalerite is well known as the main source of zinc and is a common mineral in base-metal hydrothermal mineralization. Common substitutions in the cubic polytype of the ZnS structure (β -ZnS, sphalerite) include Fe^{2+} , Mn^{2+} , and Cd^{2+} for Zn^{2+} in tetrahedral sites. Common substitutions for Zn^{2+} in the tetrahedral sites of the cubic polytype (β -ZnS, sphalerite) include Fe^{2+} , Mn^{2+} , and Cd^{2+} . Besides these major divalent cations, other minor and trace elements are found in the crystal lattice of natural sphalerites, involving coupled substitution [1,2].

ZnS polytypes, especially sphalerite and wurtzite (hexagonal α -ZnS polymorph), have been the subject of several studies dealing with geological (e.g., geobarometer [3]) and economic implications (e.g., [1]) due to the numerous substitutions that can occur in the ZnS lattice. Furthermore, ZnS is one of the most important II–VI compound semiconductors used in various domains: light-emitting or laser diodes in the Near-UV region, photocatalysis, solar energy conversion, etc. [4,5].

In recent decades, Raman spectroscopy has been used extensively for the structural and chemical characterization of sphalerites. Zigone et al. [6] reported vibrational changes in the synthetic crystals of ZnS doped with relatively small amounts of Fe, Mn, Co, or Cr. Several authors have shown the efficiency of Raman spectroscopy in quantifying

iron content in natural sphalerites [7–9]. Other systematic vibrational studies have been previously undertaken on synthetic sphalerites [10,11].

The present study investigates the potential of Raman spectroscopy for the estimation of manganese content in natural sphalerites and the effect of Mn substitution on natural sphalerites from Săcărâmb Au–Ag–Te ore deposit, found in the Metaliferi Mountains, Romania. The results have genetic implications for the Mn-rich sphalerites and a possible geological influence on sphalerite chemistry in intermediate-sulfidation (IS) and low-sulfidation (LS) ore deposits.

2. Geological Setting

The Săcărâmb Au–Ag–Te ore deposit is found in the Brad-Săcărâmb district, in the South Apuseni Mountains (Figure 1). According to thorough K–Ar analyses and stratigraphic data from earlier studies conducted by Roșu et al. [12,13], the magmatic activity in the Apuseni Mountains took place between 14.7 and 7.4 Ma, while the Săcărâmb volcanic activity took place between 10.5 and 12.8 Ma. An important feature of the Brad-Săcărâmb district is the grouping of deposits into metallogenetic nodes. The most important node is Barza, which is made up of gold and polymetallic vein groups, together with porphyry copper bodies [14]. The relationships between Miocene magmatism and extensional tectonics are thus of prime importance. The Au–Ag–Te ore is developed within over 200 veins situated in the central volcanic neck and in some andesitic necks. The volcanic structure is formed at the intersection of a group of major faults with NW–SE and E–W directions.

The morphology of the deposit was influenced by the shape of the volcanic structure and the generations of fractures that controlled the flow of fluids. The veins in the andesitic bodies in the western part of the deposit are deeper than those affiliated with lava [15].

The Săcărâmb ore deposit was described as a low-sulfidation one in [16] based on the ore and gangue mineralogy, the alteration mineral assemblages, the zonality of alterations around the ore bodies, and the geochemical associations. The fluid inclusion studies carried out on magmatic and hydrothermal quartz revealed low fluid salinities ranging from approximately 1 to 4 wt.% NaCl equiv., and low to medium homogenization temperatures ranging from 113 to 315 °C, confirming the LS character of the ore deposit with a dominance of magmatic water [17].

The Săcărâmb ore deposit has an exceedingly complex mineralogy. The primary gangue minerals are Ca–Mn carbonates, quartz, and barite. The ore minerals consist of sulfides: alabandite (Săcărâmb is the type locality), pyrite, arsenopyrite, galena, sphalerite, chalcopyrite, stibnite, and realgar. A wide variety of tellurides of Au, Ag, Pb, Sb, Bi, and Hg are found in mineralization. Săcărâmb is the type locality for a group of tellurides and Te-sulfosalts: petzite (Ag_3AuTe_2); krennerite ($Au_{1-x}Ag_xTe_2$), where ($x = 0.2 - 0.4$); stützite ($Ag_{5-x}Te_3$), where ($x = 0.24 - 0.36$); nagyágite $[Pb_3(Pb,Sb)_3S_6](Au,Te)_3$; muthmannite ($AuAgTe_2$); and museumite $[Pb_2(Pb,Sb)_2S_8](Te, Au)_2$ [16–20]. Sulfosalts are another complex part of the mineralogy of Săcărâmb, having a strong relationship with tellurides [19,20]. The most common sulfosalts are as follows: the tetrahedrite–tennantite group, the geocronite–jordanite series, bournonite and boulangerite [16,18,21]. Recently, the occurrence of luzonite–famatinitite, manganoquadratite and andorite IV, benleonardite, fullopitite, falkmanite, robinsonite, liveingite, and zinkenite in alabandite-rich mineralization has been reported [21–24]. A distinct feature of the deposit is the existence of vein groups that present similar orientations and distinctive suites of ore and gangue minerals: the Antelongothin and Ertzbau group in the NW–SE direction and the Nepomuc–Magdalena group oriented towards the NE–SW [15,25]. Paragenetic studies of individual mineralized veins have highlighted their mineralogical complexity; furthermore, the studies have revealed a succession of several mineralizing events occurring in the complex vein system [16,20,26,27].

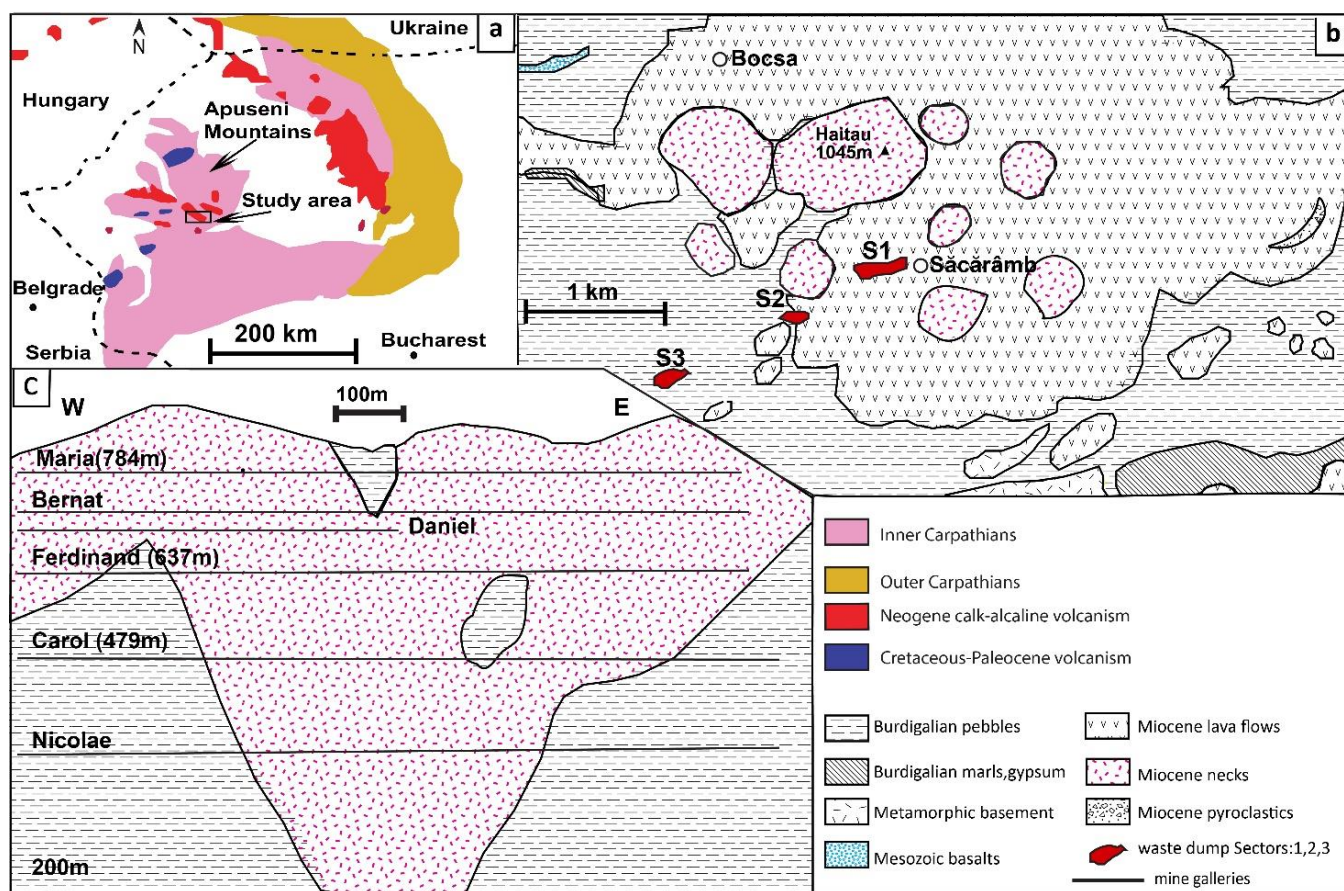


Figure 1. Localization of the studied area in the Carpathians (a); simplified geological map of Săcărâmb volcanic structure (b); simplified geologic cross-section through the Săcărâmb deposit (c), with the mining galleries redrawn after Udubaşa [18]; Alderton and Fallick [17].

3. Materials and Methods

Ore samples were collected from the surface of three waste dumps: Sector 1 (S1), Sector 2 (S2) and Sector 3 (S3) (Figure 1 shows the location of the waste dumps). Additionally, some of the studied samples were collected from a drill core, with a length of 1000 m, and positioned in the eastern part of the deposit. A total of 33 polished sections were used to identify sphalerites and texturally characterize mineral assemblages. Sphalerite identification and characterization were conducted by first observing the optical properties. The polished sections were studied under reflected light. For this part of our study, we used a Zeiss Axio Imager A2m microscope. After the optical studies, we used a scanning electron microscope with energy dispersive spectroscopy (SEM-EDS). For these observations, we used a tabletop Hitachi TM3030 SEM, operating at an accelerating voltage of 15 kV. Elemental analyses were collected through a QUANTAX 70 EDS system from Bruker.

The Raman spectra were obtained on polished sections using the micro-Raman spectrometer Renishaw InVia coupled with a Peltier cooled CCD detector. Excitation was provided by a 532 nm laser (Model: RL532C50, Renishaw, Inc., Wotton-under-Edge, UK) with a nominal power of 50 mW at room temperature. The laser power was controlled by means of a series of density filters in order to avoid heating effects. Samples were scanned from 0.5 to 1783 cm^{-1} at a nominal spectral resolution of about 1.5 cm^{-1} . The micro-Raman spectra were acquired using an exposure time of 30 s per frame, and 10–20 acquisitions at a laser power of 0.5%–1%, in order to improve the signal-to-noise ratio. Spectra were obtained using 50 \times or 20 \times magnification objectives. Calibration was performed using a 520.5 cm^{-1} line of silicon. Data acquisition was carried out using Wire software version 3.2.

The Raman spectra were reduced in intensity in order to display them clearly in stacked graphs and for a better comparison.

The abbreviations of minerals reported in the present study follow the list approved by the International Mineralogical Association (IMA) Commission on New Minerals, Nomenclature and Classification (CNMNC) [28].

4. Results

4.1. Mineral Paragenesis and Chemistry of Sphalerite

Sphalerite occurs in all mineralization stages of the deposit and predominates in the lower parts of the deposit where it is associated with common sulfides. It is isolated in massive alabandite (MnS), usually in carbonate veins. In the deeper parts of the vein system, it is one of the most common sulfides associated with galena, pyrite, and tetrahedrite. Macroscopically, two types were observed: The first type was a cleiophane sphalerite with shades of orange and yellow (Figure 2e), in which the crystals were translucent and had a resinous luster. The second type of sphalerite appeared to have a brown to black color; some crystals were opaque (marmatite) and were frequently associated with chalcopyrite and galena (Figure 2a).

Microscopically, the Săcărâmb sphalerite was differentiated into four crystallization stages. The first stage was of the marmatite type, with euhedral or subhedral crystals, often showing exsolutions of chalcopyrite, forming the so-called “chalcopyrite disease” [29] in association with pyrite, chalcopyrite, and galena (Figures 2a and 3a,b). Second-stage sphalerites occurred as inclusions in alabandite or forming assemblages with galena, tetrahedrite, and pyrite (Figures 2c,d and 3e,f). They may contain chalcopyrite inclusions but are less common than the first-stage marmatite type. In the third stage, the subhedral sphalerite (cleiophane type) predominated, with internal reflections from dark brown to yellow; it appeared in rhodochrosite veins associated with sulfosalts (bournonite and Ag-sulfosalts) or associated with sulfides (galena and pyrite), sulfosalts (bournonite–seligmannite, jordanite–geocronite, tetrahedrite, andorite, zinkenite, luzonite–famatinitite, and nagyagite), and tellurides (sylvanite, hessite, and krennerite) (Figures 2b–d and 3e,f). It frequently had inclusions of pyrite, bournonite, galena, and jordanite–geocronite, and in one sample, vermicular structures of marcasite were observed. The last crystallization stage contained anhedral crystals and, in some cases, colomorph structures were observed. This sphalerite is frequently associated with colomorph pyrite, marcasite, and Mn oxides.

The results of the chemical analyses of the sphalerites investigated are shown in Table 1, where the chemical formula was calculated on the basis of two atoms per formula unit (*apfu*). The sphalerite samples contained an extensive range of Mn (between 0 and 14.10 wt.%). Iron occurred in appreciable quantities and ranged from 0.05 wt.% to 9.48 wt.%. Cadmium contents were low (up to 0.72 wt.%), while Cu (0.16 wt.%) was found only in one analysis, probably due to the presence of micrometric chalcopyrite inclusions. Sphalerites from the Săcărâmb hydrothermal ore deposit showed an extensive transition from ferroan ($(Zn_{0.87}Fe_{0.16})_{\Sigma=1.03}S_{0.97}$) to manganoferroan ($(Zn_{0.77}Mn_{0.14}Fe_{0.06})_{\Sigma=0.97}S_{1.03}$), as well as mangan-rich ($(Zn_{0.8}Mn_{0.25})_{\Sigma=1.05}S_{0.95}$) compositions. The variation in the cation contents of natural sphalerites from the Săcărâmb ore deposit can be expressed as $Zn_{1-x}M_xS$ ($M = Mn, Fe$), where x is in the range of $0.07 \leq x \leq 0.25$.

Table 1. Chemical composition of sphalerite samples (wt.%) ordered by Mn content and the main Raman modes.

Sector/Sample Type	Samples	Mn	Fe	Cd	Cu	Zn	S	SUM	Calculated Formula	x_{Mn} (apfu)	(Mn,Fe)-S (cm ⁻¹)		LO Zn-S (cm ⁻¹)
Core sample	SGD_11_2	n.d.	4.72	n.d.	n.d.	63.11	32.18	100	$(Zn_{0.94}Fe_{0.08})_{\Sigma=1.02}S_{0.98}$	0	299	330	350
Core sample	SGD_11_1	n.d.	9.48	n.d.	n.d.	58.48	32.05	100	$(Zn_{0.87}Fe_{0.16})_{\Sigma=1.03}S_{0.97}$	0	299	330	351
Core sample	5_SGD_10_2	0.75	4	0.03	n.d.	65.42	29.8	100	$(Zn_{0.99}Fe_{0.07}Mn_{0.01})_{\Sigma=1.08}S_{0.92}$	0.01	300	331	350
Core sample	5_SGD_10_1	0.98	2.79	0.14	n.d.	63.13	32.97	100	$(Zn_{0.94}Fe_{0.05}Mn_{0.02})_{\Sigma=1.00}S_{1.00}$	0.02	300	331	348
Core sample	5_SGD_10_3	1.22	3.50	0.72	n.d.	63.85	30.71	100	$(Zn_{0.96}Fe_{0.06}Mn_{0.02})_{\Sigma=1.05}S_{0.95}$	0.02	299	330	348
Sector 3	2_S3H2_2	3.49	5.4	n.d.	n.d.	59.81	31.3	100	$(Zn_{0.89}Fe_{0.09}Mn_{0.06})_{\Sigma=1.05}S_{0.95}$	0.06	298	327	350
Sector 3	2_S3H2_1	7.22	2.23	n.d.	n.d.	58.1	32.44	100	$(Zn_{0.86}Fe_{0.04}Mn_{0.13})_{\Sigma=1.02}S_{0.98}$	0.13	297	326	349
Sector 2	8_SGD_22a_1	7.55	0.24	0.4	n.d.	59.81	32	100	$(Zn_{0.89}Mn_{0.13})_{\Sigma=1.03}S_{0.97}$	0.13	297	328	350
Sector 3	2_S3H2_3	7.92	3.57	n.d.	n.d.	53.37	35.14	100	$(Zn_{0.77}Fe_{0.06}Mn_{0.14})_{\Sigma=0.97}S_{1.03}$	0.14	298	328	350
Sector 3	4_S3K5_1	9.55	0.56	0.13	n.d.	53.28	36.48	100	$(Zn_{0.76}Fe_{0.01}Mn_{0.16})_{\Sigma=0.94}S_{1.06}$	0.16	298	327	348
Sector 3	S3I1_1_1	10.22	0.46	n.d.	n.d.	52.96	36.36	100	$(Zn_{0.76}Fe_{0.01}Mn_{0.17})_{\Sigma=0.95}S_{1.05}$	0.17	298	329	351
Sector 3	S3E4_1_4c	12.29	n.d.	0.16	n.d.	54.92	32.63	100	$(Zn_{0.81}Mn_{0.21})_{\Sigma=1.02}S_{0.98}$	0.21	298	330	352
Sector 2	SG1_1_3	13.11	0.05	0.28	0.16	53.50	32.90	100	$(Zn_{0.78}Mn_{0.23})_{\Sigma=1.02}S_{0.98}$	0.23	297	328	350
Sector 3	S3E4_1_4b	13.74	n.d.	0.49	n.d.	53.96	31.81	100	$(Zn_{0.8}Mn_{0.24})_{\Sigma=1.04}S_{0.96}$	0.24	295, 307 sh	328	349
Sector 3	S3E4_1_4	14.10	0.24	0.03	n.d.	54.23	31.40	100	$(Zn_{0.8}Mn_{0.25})_{\Sigma=1.05}S_{0.95}$	0.25	295, 307 sh	326	350

Structural formula calculated in atoms per formula unit (apfu) based on $\Sigma_{atoms} = 2$; n.d. = not detected; sh—shoulder Raman peak.

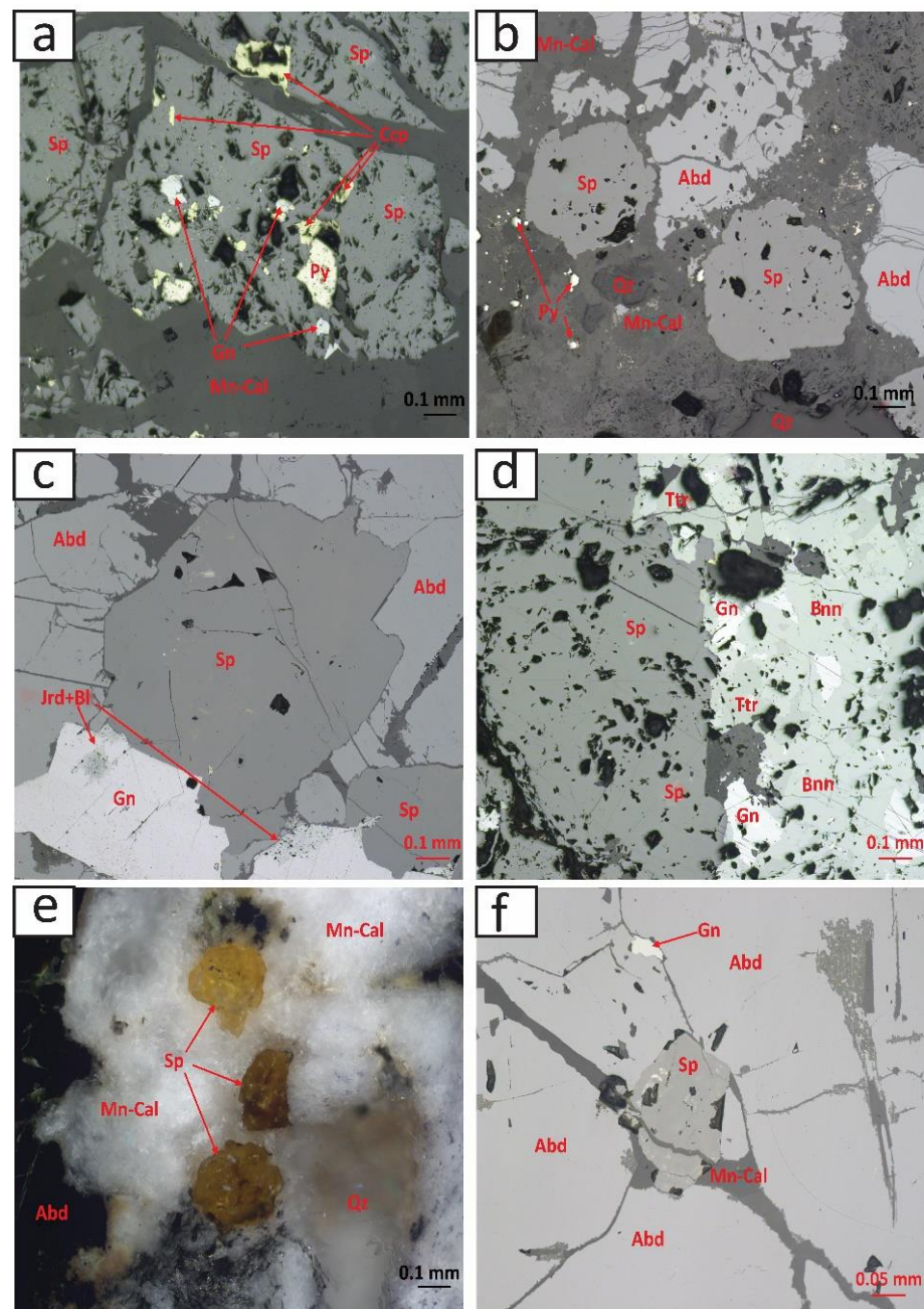


Figure 2. Photomicrographs of the samples observed under reflected light (a–f): (a) sphalerite with chalcopyrite (Ccp) and pyrite (Py) inclusions; (b) subhedral sphalerite crystals in a Mn-rich calcite and quartz vein replacing alabandite; (c–f) sphalerite crystals in massive alabandite in association with galena (Gn), jordanite (Jrd), and bernarlottite (Bl); (d) sphalerite with galena, tetrahedrite (Ttr) and bournonite (Bnn); (e) cross-polarized image of sphalerite crystals (Sp) presenting yellow internal reflections in association with alabandite (Abd), Mn-rich calcite (Mn-Cal), and quartz (Qz).

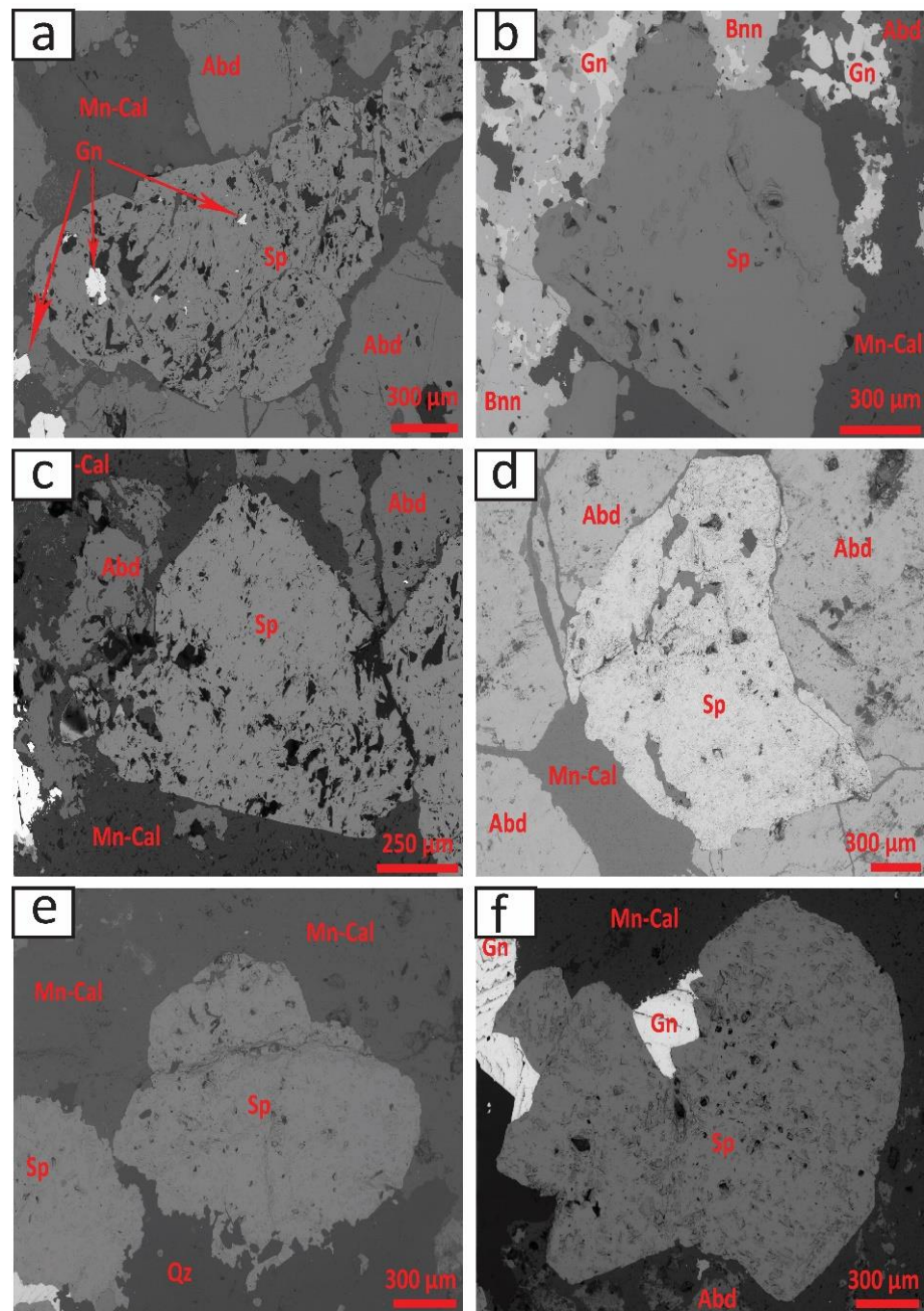


Figure 3. SEM backscattered images of sphalerite (Sp), where: (a,b) stage III sphalerite associated with galena (Gn) and bournonite (Bnn); (c,d) stage II sphalerite in association with alabandite (Abd); (e,f) stage I sphalerite in Mn-rich calcite (Mn-Cal) and quartz (Qz) veins, in association with galena.

4.2. Raman Spectroscopy and Band Assignments

The Raman spectra of the natural sphalerite samples from the Săcărâmb ore deposit showed typical first-order Raman modes with the main peaks at ~ 350 , ~ 330 , and ~ 300 (dominant) cm^{-1} . Figure 4 shows the Raman spectra of $\text{Zn}_{1-x}\text{Mn}_x\text{S}$ with x in the range $0 \leq x \leq 0.25$ (Table 1). To the best of our knowledge, Raman data for natural Mn-rich sphalerite have not been published so far.

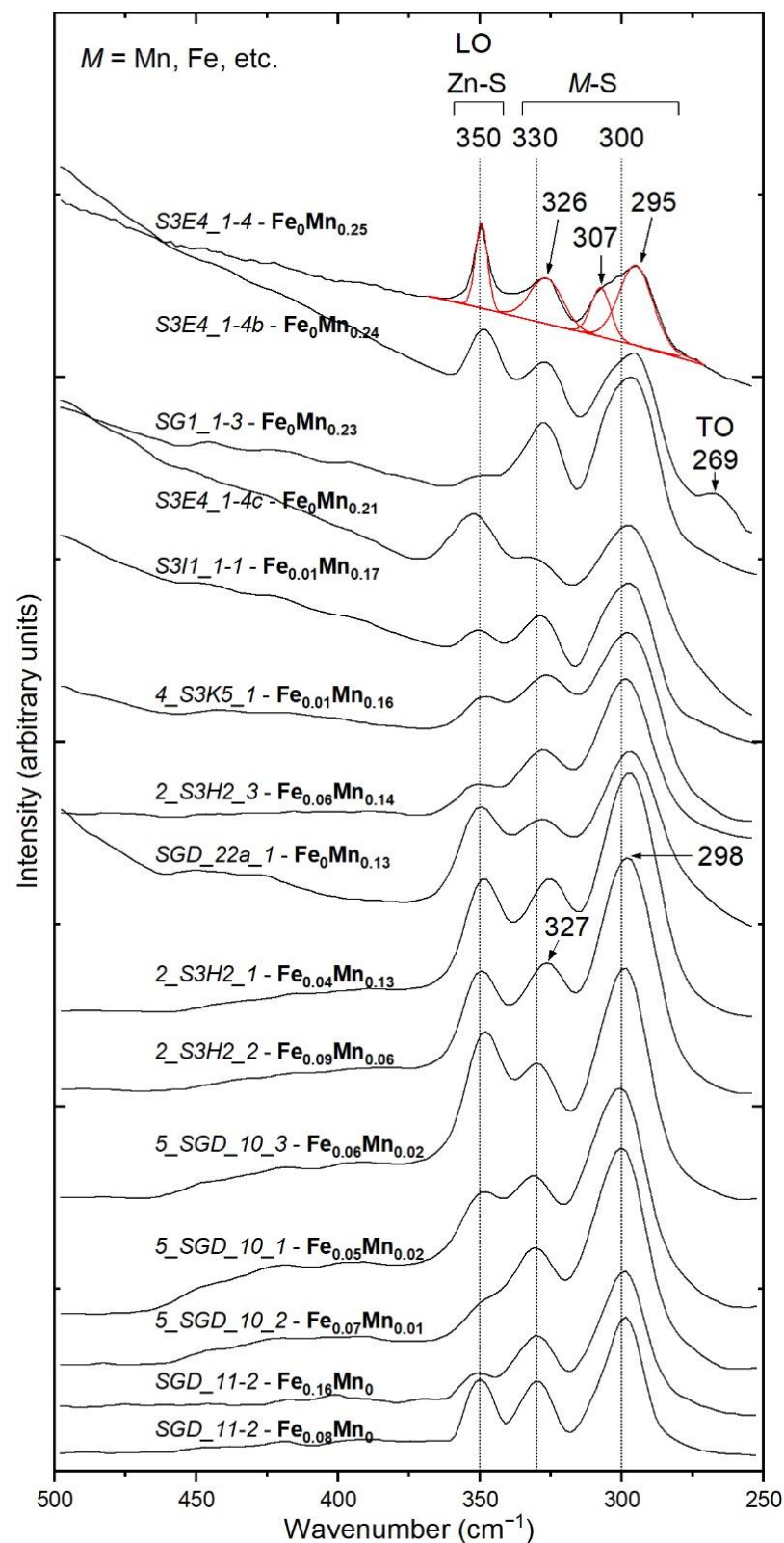


Figure 4. Raman spectra of the natural sphalerite samples from the Săcărâmb ore deposit. The spectra are displaced vertically for clarity. The red line represents the deconvolution with Gaussian fitting for sample S3E4_1-4 with $x_{\text{Mn}} = 0.25$.

The assignment of the Raman modes was based on previous studies [7,8,30], where the LO mode (longitudinal optical) occurred at $\sim 350 \text{ cm}^{-1}$ and was due to the Zn–S vibration,

while the Raman bands located at ~ 330 and ~ 300 cm^{-1} were assigned to metal–sulfur modes (i.e., (Mn,Fe)-S vibrations). The deconvolution process with Gaussian fitting revealed an additional mode for the Mn-rich Raman spectra, where a shoulder arose at 307 cm^{-1} (Figure 4).

The transverse optical (TO) mode arose only in one sample (S3E4_1-4b, Figure 4) at 269 cm^{-1} . The Raman spectral domain was truncated to 500 – 250 cm^{-1} due to the lower intensities of the acoustic modes (longitudinal and transverse (LA and TA), i.e., below 250 cm^{-1}) and the combination modes, which arose at above 500 cm^{-1} .

5. Discussion

5.1. Vibrational Characteristics of Mn-Substituted Sphalerite

In recent years, several Raman studies on natural [7–9] and synthetic [10,11] sphalerites have pointed out systematic changes in spectroscopic parameters (e.g., peak shifts and changes in relative intensity) due to the simple substitution of divalent ions for Zn in sphalerite lattice sites. Moreover, a detailed spectroscopic investigation was carried out by Zigone et al. [6] on ZnS synthetic crystals containing a small concentration ($\approx 1\%$) of transition elements, such as Fe, Mn, Co, Cr, and Ni. They found that the frequencies of all new modes were found between LO and TO modes (i.e., impurity-induced modes), and showed small differences in the measured frequencies for each of the above-mentioned elements. These small differences can be attributed to the electronegativity [9] and mass differences [10] of the cation substituted. Babedi et al. [11] established a relation between the electronegativity of Fe, Mn, and Cd, versus the Raman peak located at around 300 cm^{-1} . Taking into account several vibrational studies on sphalerite containing variable amounts of Mn, Cr, Cd, Fe, Co, and Ni [6,8–11], a strong correlation between the electronegativity of the consequent metal–sulfide bond and Raman mode position can be extended as shown in Figure 5. However, despite the lack of Raman data for sphalerites with indium and copper, the wavenumber of these elements was inferred from the fit line ($r = 0.91$).

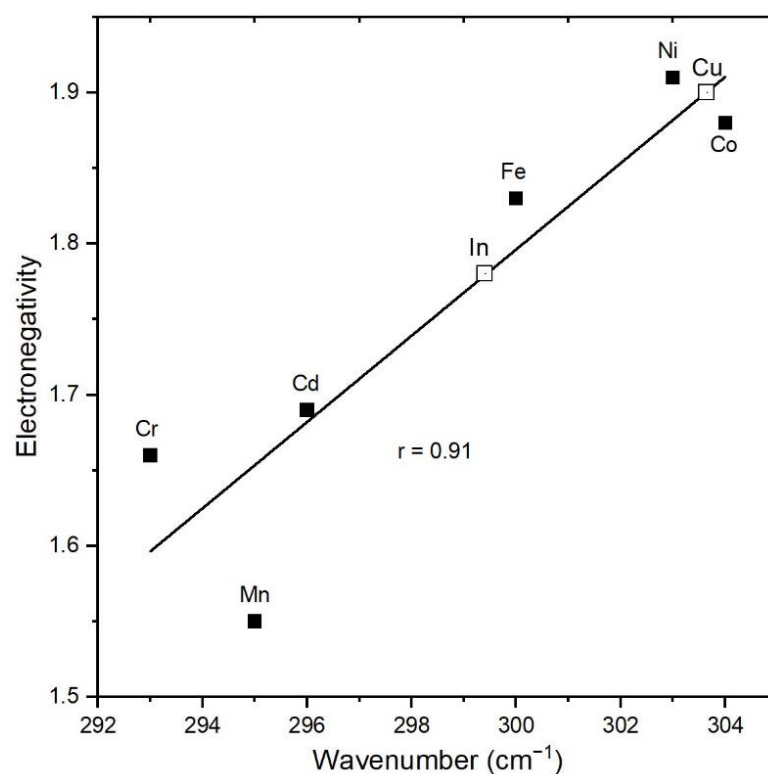


Figure 5. Electronegativity of different divalent ions that substitutes Zn in sphalerite lattice sites vs. the Raman mode position of the consequent metal–sulfide bond.

For the sphalerite samples with an iron content up to 9.48 wt.% (Figure 4), the relative intensities are consistent with Kharbish [8] and Buzatu et al. [9], who found that iron content can be quantified by measuring the relative intensities and intensity ratios of the following Raman modes: 350, 330, and 300 cm^{-1} . In our study, the manganoferroan and Mn-rich sphalerites did not show any change in terms of the relative intensities of any Raman mode as a function of Mn concentration. Jiménez-Sandoval et al. [10] also showed that both the intensities and frequencies of the TO and LO modes of synthetic $\text{Zn}_{1-x}\text{Mn}_x\text{S}$ with different Mn ($0 < x < 0.5$) were independent of the Mn concentration. However, Jiménez-Sandoval et al. [10] highlight variations in the relative intensities and line widths of the impurity-induced modes at 300, 312, and 332 cm^{-1} .

In this study, the peak positions of the natural Mn-rich sphalerite were observed to vary with the composition (Figure 4) across an extended domain of $\text{Zn}_{1-x}\text{Mn}_x\text{S}$ with x in the range $0 \leq x \leq 0.25$. The observed range of peak positions was ~5 wavenumbers: from 300 cm^{-1} (sample #SGD_11_2, $x_{\text{Mn}} = 0$) to 295 cm^{-1} (sample #S3E4_1_4, $x_{\text{Mn}} = 0.25$). This shifting behavior started with contents exceeding 3 wt.% Mn ($x_{\text{Mn}} = 0.06$). Moreover, the peak became broader with increasing manganese content. Figure 6 shows a strong negative correlation ($r = -0.84$) between manganese content and the Raman wavenumbers. Exploiting this relationship, the following linear equation of the first-order polynomial fit was obtained:

$$x_{\text{Mn}} = (\omega_0 - 300.03013) \div -0.16375 \quad (r = -0.84) \quad (1)$$

where ω_0 is the wavenumber value of the Raman band, and x_{Mn} is the manganese content expressed in atom per formula unit (apfu).

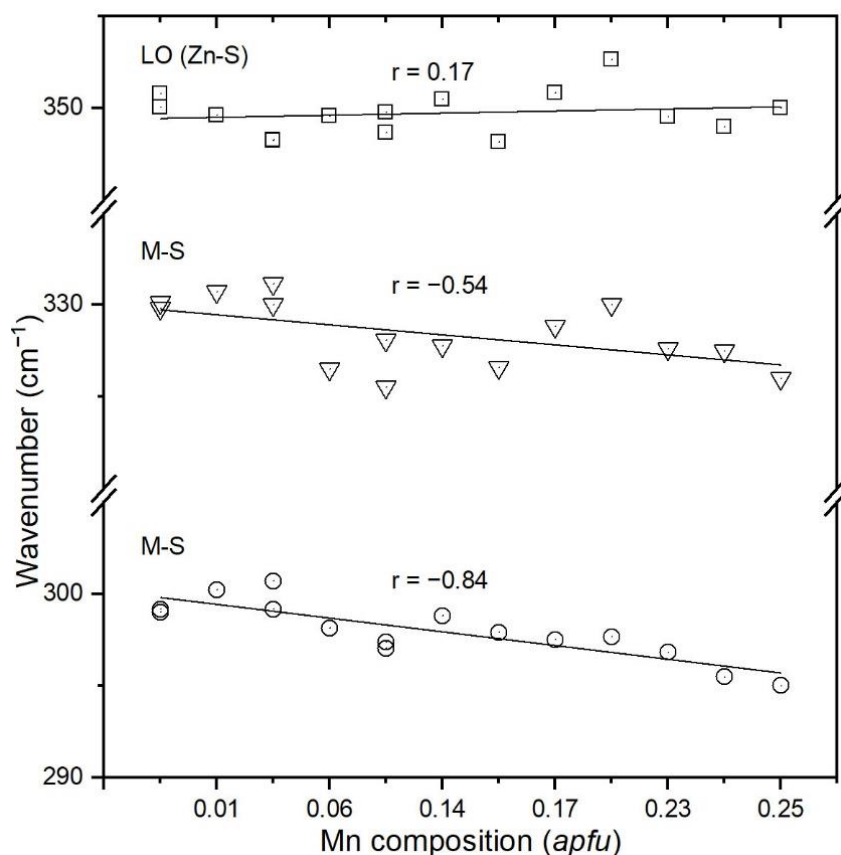


Figure 6. Correlation between Raman bands position (cm^{-1}) and the Mn composition (apfu) of the sphalerite from the Săcărâmb ore deposit.

Due to the nature of the samples used in this study, most of the samples had mixed compositions of $\text{Mn} \pm \text{Fe}$ with $\text{Zn}_{1-x}\text{M}_x\text{S}$ ($M = \text{Mn}, \text{Fe}$), where x is in the range of $0.07 \leq x \leq 0.25$. As previous studies [8,9] have already confirmed that iron contents do

not exhibit the behavior described above, we postulate that the shift of the Raman peak is due to the increase in Mn content. Moreover, it is worth mentioning that Zn correlates negatively with Mn + Fe (correlation coefficient: $r = -0.92$; Figure 7a), suggesting that it is replaced by both of them. Furthermore, Mn inversely correlates with Fe ($r = -0.81$, Figure 7b). In natural sphalerites, the lattice is a dynamic system where different cations, especially transition metals with a variable number of 3d electrons, are involved in the hydrothermal fluids (i.e., Mn— $3d^5$, Fe— $3d^6$). Fregola et al. (2012) show that the presence of transition elements with unpaired external electronic levels can cause large distortions in tetrahedral and octahedral sites of spinel (belonging to the $(Mg_{1-x}Cu_x)Al_2O_4$ series) due to the Jahn–Teller (JT) effect. It is worth mentioning the influence of the JT effect at tetrahedral site $Fe^{2+}O_4$ in the structure of chromite [31], or in ferro-magnesian minerals [32]. The influence of the isomorphic substitution of zinc with other divalent cations (M^{2+}) in the tetrahedral site causes an increase in the reticular parameter a of the sphalerite unit cell with increasing metal content [9,11,30,33,34], which is responsible for the structural distortions in sphalerite lattice. Moreover, Vallin et al. [35] demonstrated the presence of JT effects in the ZnS lattice, due to Cr^{2+} impurity centers. The different vibrational behavior between Mn-doped samples of sphalerite [10] and natural Mn-rich sphalerite from the present study would be a result of the nature of the samples or due to the resolution of the spectrometer.

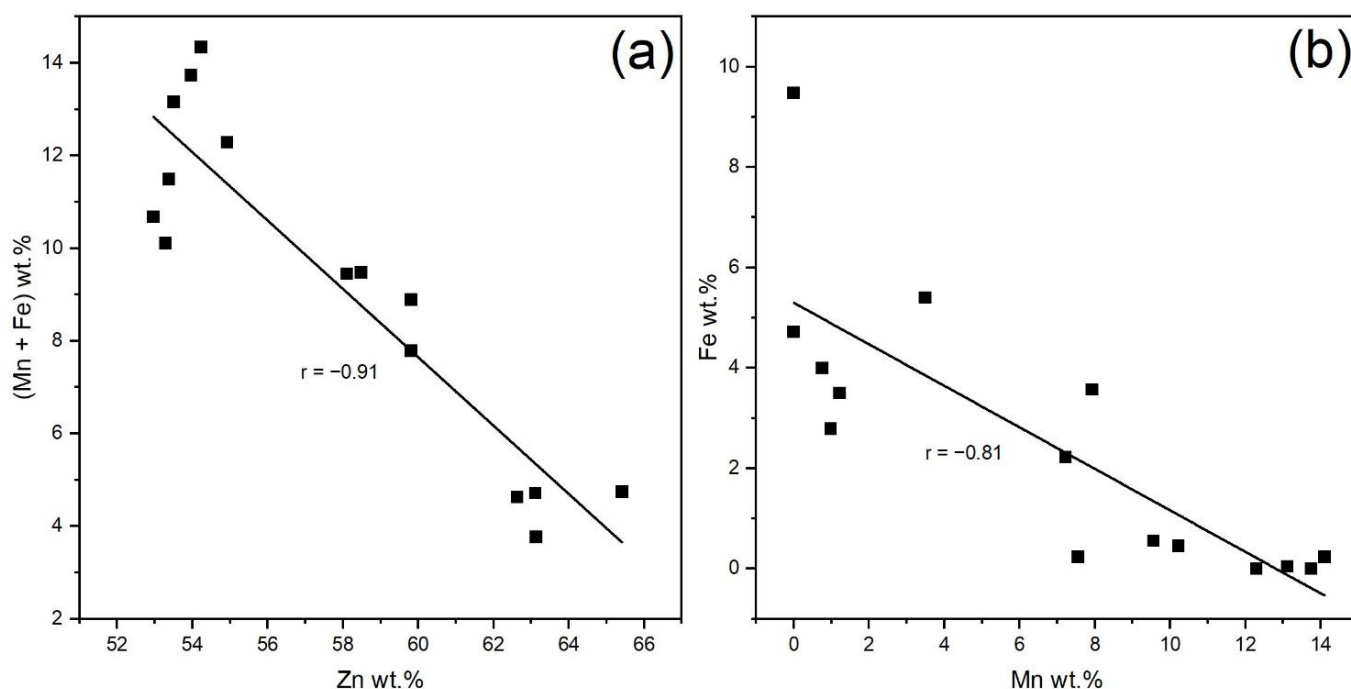


Figure 7. (a) Correlation between Zn and Mn + Fe (wt.%); (b) correlation between Mn and Fe (wt.%) in sphalerites from the Săcărâmb ore deposit.

This systematic peak-position shift towards lower wavenumbers with increasing Mn content is mainly linked to the smaller ionic radius of Mn^{2+} (i.e., Mn^{2+} has a smaller ionic radius than Zn^{2+}) and polyhedral distortions in tetrahedral sites (MnS_4), where the symmetry reduces from T_d to D_{2d} . The local displacement of atoms in the crystal lattice of natural sphalerites induced by Mn^{2+} ions is strongly related to the nature of the samples and the physicochemical conditions during the precipitation and recrystallization of sphalerite.

Another argument for a reduction in symmetry consists of the splitting of the 300 cm^{-1} (295 cm^{-1} and the shoulder located at 307 cm^{-1} ; Figure 4) as a function of Mn concentration starting with 13 wt.% Mn ($x_{Mn} = 0.23$). These polyhedral distortions are also responsible for the widening of the Raman peaks of the Mn-rich sphalerites, located at 295 cm^{-1} . A similar interpretation can be drawn for the synthetic sphalerites doped with Cd, where

Babedi et al. [11] identify a new mode (i.e., “X mode” located at 295 cm^{-1}), which increases in intensity as a function of Cd concentration. Similar shifting and broadening for the LO and TO modes was observed by Nien and Chen [36] at different Cu concentrations in synthetic sphalerite lattice, who attributed this behavior to the interstitial location of the Cu ions.

In addition, a moderate negative correlation ($r = -0.54$) between manganese content and the Raman wavenumbers was also observed for the Raman peak located at $\sim 330\text{ cm}^{-1}$ (Figure 4). The observed range of peak positions was ~ 4 wavenumbers: from 330 cm^{-1} (sample #SGD_11_2, $x_{Mn} = 0$) to 326 cm^{-1} (sample #S3E4_1_4, $x_{Mn} = 0.25$). This shifting behavior started with contents exceeding 1.22 wt.% Mn ($x_{Mn} = 0.02$). Therefore, the Mn content can be quantified (in *apfu*) by using the following linear equation:

$$x_{Mn} = (\omega_1 - 330.52448) \div -0.26516 \quad (r = -0.54) \quad (2)$$

where ω_1 is the wavenumber value of the Raman band, and x_{Mn} is the manganese content expressed in atom per formula unit (*apfu*).

On the other hand, the wavenumber of the LO mode located at 350 cm^{-1} is not a function of the Mn content. The Raman peak located at 326 cm^{-1} is close to the frequency of the so-called “B mode” (i.e., breathing mode) observed by Jiménez-Sandoval et al. [10] at 328 cm^{-1} . They noticed that the frequency of this mode remains constant, and its intensity increases as the manganese content increases.

According to Sombuthawee et al. [37], the MnS incorporation in the galena-type sphalerite structure is limited to 7 mol.%. In contrast, wurtzite (a high-temperature polymorph of sphalerite) can absorb ~ 50 mol.% almost without temperature dependence [38]. To the best of our knowledge, this is the highest Mn content (up to 14.1 wt.%) in sphalerite reported within the Golden Quadrilateral ore deposits (up to 6.01 wt.% at Roşia Montană [39]) and the Baia Mare mining district (0.86 wt.% at Şuitor [40]). Previously, Cook et al. [1] reported up to 6.75 wt.% in Săcărâmb hydrothermal ore deposit. To date, higher contents of manganese in sphalerite have been found in Ag-rich Santo Toribio epithermal deposits (up to 14.5 wt.%; [41]) and the Tisovec skarn (up to 21.38 wt.%; [42]).

A moderate correlation ($r = 0.51$) between Fe and Mn was found by Damian et al. [40] in hydrothermal sphalerites from ore deposits from the Baia Mare area. Cook et al. [1] also reported a weak positive correlation between these two elements, mainly in individual ore deposits or sample subsets. The linear correlation between Mn and Fe (i.e., $r = -0.81$) in the sphalerites from Săcărâmb suggests the competitive character of these divalent metals in the mineral–fluid interface. The substitution of $\text{Zn}^{2+} \leftrightarrow \text{Mn}^{2+}$ is accompanied by $\text{Zn}^{2+} \leftrightarrow \text{Fe}^{2+}$ substitution, and vice versa. Di Benedetto [43] showed that the presence of Mn strongly depends on the Fe content in zoned crystals of sphalerites. They proposed that the competition between Mn and Fe for the replacement of Zn is an internally controlled mechanism during crystal growth, where Cd may influence the distribution of both Fe and Mn. In the present study, ore microscopy and chemical analyses revealed the presence of homogeneous sphalerite crystals, without compositional zoning and a neglectable low Cd concentration (<0.72 wt.% Cd).

5.2. Implications for Metallogenesis of the Săcărâmb Ore Deposit

Based on our investigation and previous studies [15–17,20], the mineralization stages of the Săcărâmb Au–Ag–Te deposit can be summarized as follows:

- Stage I is a high-temperature stage between 400 and $500\text{ }^{\circ}\text{C}$, dominated by common sulfides disseminated in the altered andesitic neck.
- Stage II is characterized by temperatures between 350 and $400\text{ }^{\circ}\text{C}$; it is a more complex stage with the presence of sulfosalts and the development of vein systems,
- Stage III is a Mn-rich stage; it is considered the main ore formation stage with temperatures between 200 and $300\text{ }^{\circ}\text{C}$, and alabandite as the main sulfide mineral, forming

veins of up to 10 cm in diameter. In this stage, sphalerite crystals with the highest Mn content were identified.

- Stage IV is a telluride- and sulfosalt-rich stage with lower temperatures between 150 and 230 °C, as presented by Dincă [20]. Sphalerite in this stage has a high Mn concentration as in stage III; however, Fe and Cd are present in the composition.
- Stage V, the oxide and As-Sb stage, is the final mineralization stage in which glauco-type ore is present with Mn oxides, realgar, orpiment, stibnite, and native Au. The formation temperature is between 100 and 150 °C.

The Mn concentrations in sphalerite are strongly affected by redox conditions [44,45], with high Mn generally reflecting a reduced environment [45,46]. Variations in MnS content in sphalerite may reflect variations in the activity of MnS in the fluid and in physicochemical conditions during precipitation. Additionally, variation in the mol.% MnS of sphalerite coexisting with alabandite reflects the variability of the sulfidation state.

The precipitation and recrystallization of sphalerite presumably occurred under similar Eh-pH conditions as alabandite. The non-separation of Mn from Fe might have resulted from low Eh, which kept Mn and partly Fe in a divalent state, thus enabling the primary formation of Mn–Fe-rich sphalerite in stages II and III (Figure 8, type 3). It is suggested that in nature, the presence of Mn-rich sphalerite is strongly related to the cogenetic Mn minerals associated with ore deposits. Mn-rich sphalerites have been discovered in two types of hydrothermal deposits: (i) Mn skarn deposits, in which the sphalerites are associated with Mn–Fe spinels, Mn carbonates, and alabandite [42,47]; and (ii) in epithermal Au–Ag deposits in association with alabandite and Mn carbonates [20,39,41]. The presence of Mn carbonates (i.e., rhodochrosite and manganocalcite) is a common diagnostic feature to discern IS from LS epithermal deposits [48,49].

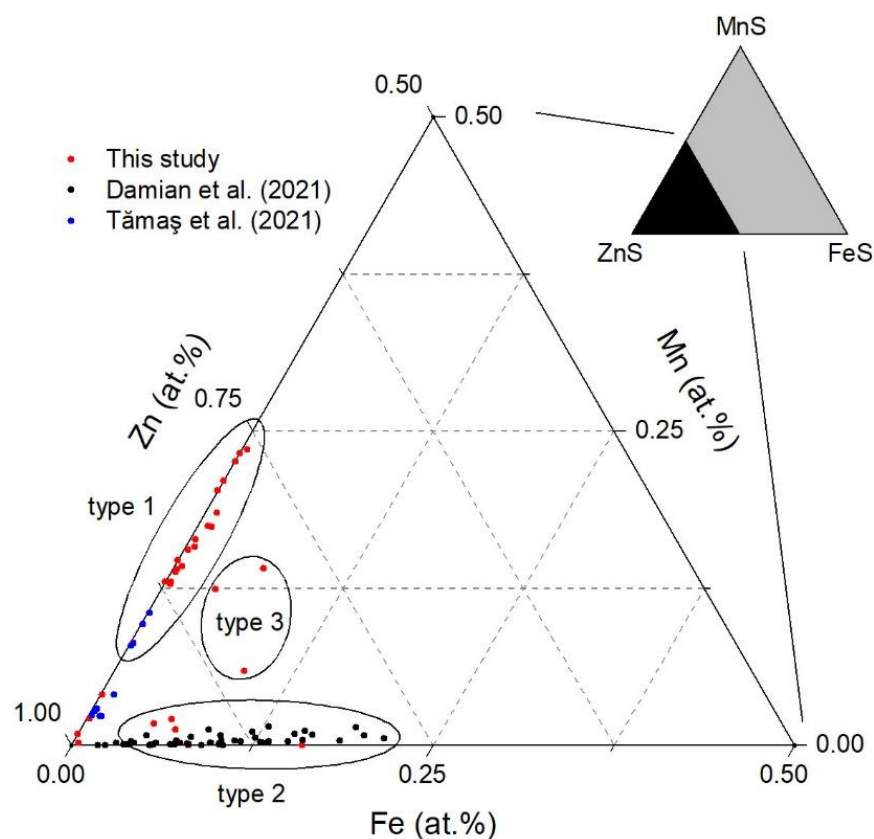


Figure 8. Zn–Mn–Fe ternary diagram showing the chemistry (expressed in at.%) of the main genetic types of sphalerites from three epithermal ore deposits from Romania: Săcărâmb (this study), Baia Mare area [40], and Roșia Montană [39].

In the case of the Săcărâmb ore deposit, one of the reasons for variable concentrations of Mn, Fe, and Cd in sphalerites could be the fluid throttling and boiling at stages III and IV, induced by the vertical ascent of hydrothermal fluid combined with the interaction with the sedimentary and volcanic rocks [16]. However, the principal connection between Mn and sphalerite consists of the presence of alabandite as the main source of Mn. Based on the spatial relationships and textural characteristics between alabandite and sphalerites, it can be suggested that two types of formation processes have been involved in Mn enrichment. The first process was the hydrothermal coprecipitation of alabandite with Mn-sphalerite, galena, tellurides, and Pb-Sb/As sulfosalts in a low-sulfidation environment (Figure 8, type 1). A sulfide resurgence induced the second formation process in a carbonate-rich and low-sulfur fluid that dissolved the main Mn ore and reprecipitated a more chemically complex sphalerite in association with pyrite, galena Ag-Cu sulfosalts, tellurides, and alabandite (Figure 8, type 3).

6. Conclusions

The following conclusions can be drawn:

1. Natural sphalerites of $Zn_{1-x}M_xS$ ($M = \text{Mn, Fe}$), where x is in the range of $0.07 \leq x \leq 0.25$, were analyzed by means of SEM-EDS and Raman spectroscopy. The sphalerite samples contain an extensive amount of Mn (between 0 and 14.10 wt.%), which is the largest concentration of Mn in sphalerites from Romanian territory.
2. New Raman spectra of natural Mn-rich sphalerites are presented for the first time. The results obtained in the present study provide Mn estimation by determining the positions of the 330 and 300 cm^{-1} Raman bands. Accordingly, two linear equations were obtained. In this regard, the present study has revealed the usefulness of Raman spectroscopy for (semi)quantitative measurements of Mn concentration in natural sphalerites.
3. This systematic peak-position shift towards lower wavenumbers with increasing Mn content is mainly linked to the smaller ionic radius of Mn^{2+} and polyhedral distortions in tetrahedral sites (MnS_4) where the symmetry reduces from T_d to D_{2d} .
4. In this study, three genetic types of sphalerites were identified: from ferroan ($(\text{Zn}_{0.87}\text{Fe}_{0.16})_{\Sigma=1.03}\text{S}_{0.97}$) to manganferroan ($(\text{Zn}_{0.77}\text{Mn}_{0.14}\text{Fe}_{0.06})_{\Sigma=0.97}\text{S}_{1.03}$), as well as mangan-rich ($(\text{Zn}_{0.8}\text{Mn}_{0.25})_{\Sigma=1.05}\text{S}_{0.95}$) compositions.
5. Mn-sphalerites are strongly connected to the presence of alabandite in mineralized assemblages.
6. The formation of several types of sphalerites in the Săcărâmb Au–Ag–Te ore deposit was caused by the succession of different types of hydrothermal fluids and the interaction between the fluids and the host material (host rocks and earlier mineralized stages).

Author Contributions: Conceptualization, G.D. and A.I.A.; methodology, G.D., A.I.A. and A.E.M.; software, A.I.A. and G.D.; validation, G.D. and R.S.; formal analysis, G.D.; investigation, G.D. and R.S.; resources, G.D.; data curation, G.D.; writing—original draft preparation, G.D. and A.I.A.; writing—review and editing, A.E.M., R.S., G.D. and A.I.A.; visualization, A.I.A., G.D. and A.E.M.; supervision, G.D.; project administration, G.D. All authors have read and agreed to the published version of the manuscript.

Funding: The APC was funded by the Romanian Ministry of Research, Innovation and Digitization, within Program 1—Development of the national RD system, Subprogram 1.2—Institutional Performance—RDI excellence funding projects, contract no.11PFE/30.12.2021.

Data Availability Statement: Not applicable.

Acknowledgments: Authors are thankful to the Romanian Ministry of Research, Innovation and Digitization, within Program 1—Development of the national RD system, Subprogram 1.2—Institutional Performance—RDI excellence funding projects, contract no.11PFE/30.12.2021, for financial support. The authors gratefully acknowledge the staff of Eldorado Gold Corporation for providing access to the Săcărâmb ore dumps and for access to drill cores. We also thank the Geoecolab Laboratory, Geological Institute of Romania, for access to SEM-EDS and the Raman spectrometer. Data processing and the writing of the paper were performed within the national projects RESET, PN-III-P2-2.1-PED-2019-453 and RoQ-Stone—PN19-45-02-01. We extend our gratitude also to the anonymous reviewers for their time spent reading the first draft of our manuscript and for their valuable suggestions. We would also like to thank Panagiotis Voudouris for his valuable comments, which helped to improve the final version of the manuscript.

Conflicts of Interest: The authors declare no conflict of interest.

References

1. Cook, N.J.; Ciobanu, C.L.; Pring, A.; Skinner, W.; Shimizu, M.; Danyushevsky, L.; Saini-Eidukat, B.; Melcher, F. Trace and minor elements in sphalerite: A LA-ICPMS study. *Geochim. Cosmochim. Acta* **2009**, *73*, 4761–4791. [\[CrossRef\]](#)
2. Pring, A.; Wade, B.; McFadden, A.; Lenehan, C.E.; Cook, N.J. Coupled Substitutions of Minor and Trace Elements in Co-Existing Sphalerite and Wurtzite. *Minerals* **2020**, *10*, 147. [\[CrossRef\]](#)
3. Scott, S.D. Experimental Calibration of the Sphalerite Geobarometer. *Econ. Geol.* **1973**, *68*, 466–474. [\[CrossRef\]](#)
4. D’Amico, P.; Calzolari, A.; Ruini, A.; Catellani, A. New energy with ZnS: Novel applications for a standard transparent compound. *Sci. Rep.* **2017**, *7*, 16805. [\[CrossRef\]](#)
5. Voigt, D.; Sarpong, L.; Bredol, M. Tuning the Optical Band Gap of Semiconductor Nanocomposites—A Case Study with ZnS/Carbon. *Materials* **2020**, *13*, 4162. [\[CrossRef\]](#) [\[PubMed\]](#)
6. Zigone, M.; Vandevyver, M.; Talwar, D.N. Raman scattering and local force variations due to transition-element impurities in zinc-sulfide crystals: Effect of pressure application. *Phys. Rev. B* **1981**, *24*, 5763. [\[CrossRef\]](#)
7. Hope, G.A.; Woods, R.; Munce, C.G. Raman microprobe mineral identification. *Miner. Eng.* **2001**, *14*, 1565–1577. [\[CrossRef\]](#)
8. Kharbish, S. A Raman spectroscopic investigation of Fe-rich sphalerite: Effect of Fe-substitution. *Phys. Chem. Miner.* **2007**, *34*, 551–558. [\[CrossRef\]](#)
9. Buzatu, A.; Buzgar, N.; Damian, G.; Vasilache, V.; Apopei, A.I. The determination of the Fe content in natural sphalerites by means of Raman spectroscopy. *Vib. Spectrosc.* **2013**, *68*, 220–224. [\[CrossRef\]](#)
10. Jiménez-Sandoval, S.; López-Rivera, A.; Irwin, J.C. Influence of reduced mass differences on the Raman spectra of ternary mixed compounds: $\text{Zn}_{1-x}\text{Fe}_x\text{S}$ and $\text{Zn}_{1-x}\text{Mn}_x\text{S}$. *Phys. Rev. B* **2003**, *68*, 054303. [\[CrossRef\]](#)
11. Babedi, L.; von der Heyden, B.P.; Neethling, P.H.; Tadie, M. The effect of Cd-substitution on the Raman vibrational characteristics of sphalerite. *Vib. Spectrosc.* **2019**, *105*, 102968. [\[CrossRef\]](#)
12. Roșu, E.; Pécskay, Z.; Ștefan, A.; Popescu, G.; Panaiotu, C.; Panaiotu, C.E. The evolution of the Neogene volcanism in the Apuseni Mountains (Romania): Constraints from new K-Ar data. *Geol. Carpathica* **1997**, *48*, 353–359.
13. Roșu, E.; Seghedi, I.; Downes, H.; Alderton, D.H.; Szakács, A.; Pécskay, Z.; Panaiotu, C.; Panaiotu, C.E.; Nedelcu, L. Extension-related Miocene calc-alkaline magmatism in the Apuseni Mountains, Romania: Origin of magmas. *Swiss Bull. Mineral. Petrol.* **2004**, *84*, 153–172.
14. Popescu, G.C.; Neacșu, A.; Cioacă, M.E.; Buia, G. Tellurium, Selenium and Cadmium Resources in the Waste Dumps of Săcărâmb Area (Apuseni Mountains), Romania. A Preliminary Estimation. *Earth Environ. Sci.* **2013**, *8*, 199–206.
15. Ianovici, V.; Borcoș, M.; Bleahu, M.; Patrulius, D.; Lupu, M.; Dimitrescu, R.; Savu, H. *Geology of the Apuseni Mountains*; Editura Academiei Române: București, Romania, 1976.
16. Ciobanu, C.; Cook, N.; Damian, G.; Damian, F.; Buia, G. Telluride and sulphosalt associations at Sacarimb. In *Proceedings of the Au-Ag-Telluride Deposits of the Golden Quadrilateral, Apuseni Mts., Romania*; Guidebook Intern. Field Workshop of IGCP Proj; Schweizerbart Science Publishers: Stuttgart, Germany, 2004; pp. 145–186.
17. Alderton, D.H.; Fallick, A.E. The nature and genesis of gold-silver-tellurium mineralization in the Metaliferi Mountains of western Romania. *Econ. Geol.* **2000**, *95*, 495–516. [\[CrossRef\]](#)
18. Udubasa, G. Excursion Guide. Mineral Occurrences in the Metaliferi Mountains, Romania. *Rom. J. Miner.* **1992**, *75*, 35p.
19. Dincă, G.; Popescu, G.; Ciobotea-Barbu, O.C. New data on the relationship between alabandite and Te-minerals from Săcărâmb Au-Ag-Te ore deposit. In *Proceedings of the Ore Deposits of Asia: China and Beyond*, SEG, Beijing, China, 17–20 September 2017.
20. Dincă, G. Mineralogia Zăcămintului de Au-Ag-Te Săcărâmb, cu Privire Specială Asupra Sulfosărilor. Ph.D. Thesis, University of Bucharest, Bucharest, Romania, 2019.
21. Dincă, G.; Popescu, G.C.; Bîrgăoanu, D.; Ciobotea-Barbu, O.C. Pb-Sb/As sulfosalts from Săcărâmb Au-Ag-Te ore deposit (Romania). In *Proceedings of the Life with Ore Deposits on Earth—15th SGA*, Glasgow, UK, 27–30 August 2019; pp. 1800–1803.
22. Dincă, G.; Popescu, G.C.; Ciobotea-Barbu, O.C.; Bîrgăoanu, D. Silver sulfotellurides and other te-sulfosalts in alabandite-bearing veins from Săcărâmb Au-Ag-Te ore deposit, Metaliferi Mountains, Romania. *Rom. J. Miner. Depos.* **2018**, *91*, 19–24.

23. Dincă, G.; Popescu, G.C. New sulfosalt associations from Săcărâmb Au-Ag-Te ore deposit. Preliminary Data. *Rom. J. Miner. Depos.* **2016**, *89*, 65–70.
24. Dincă, G.; Popescu, G.C. Manganocubite and Cd-manganocubite from Săcărâmb Au-Ag-Te ore deposit, Metaliferi Mountains, Romania. *Carpathian J. Earth Environ. Sci.* **2019**, *14*, 131–136. [\[CrossRef\]](#)
25. Ghitulescu, T.; Socolescu, M. *Etude Géologique et Minière des Monts Métallifères: (Quadrilatère, Aurifère et Régions Environnantes)*; Imprimeria Națională: București, Romania, 1941.
26. Giuscă, D. Note préliminaire sur la genèse du gisement aurifère de Săcărâmb. *Bul. Lab. Min. Gen. Univ. Buc.* **1935**, *1*, 72–82.
27. Giuscă, D. La genèse du gisement aurifère de Săcărâmb. *C. R. Acad. Sci. Roum.* **1936**, *1*, 243–246.
28. Warr, L.N. IMA–CNMNC approved mineral symbols. *Mineral. Mag.* **2021**, *85*, 291–320. [\[CrossRef\]](#)
29. Barton, P.B.; Bethke, P.M. Chalcopyrite disease in sphalerite; pathology and epidemiology. *Am. Mineral.* **1987**, *72*, 451–467.
30. Osadchii, E.G.; Gorbatiy, Y.E. Raman spectra and unit cell parameters of sphalerite solid solutions (Fe_xZn_{1-x}S). *Geochim. Cosmochim. Acta* **2010**, *74*, 568–573. [\[CrossRef\]](#)
31. Kyono, A.; Gramsch, S.A.; Yamanaka, T.; Ikuta, D.; Ahart, M.; Mysen, B.O.; Mao, H.-K.; Hemley, R.J. The influence of the Jahn–Teller effect at Fe²⁺ on the structure of chromite at high pressure. *Phys. Chem. Miner.* **2011**, *39*, 131–141. [\[CrossRef\]](#)
32. Walsch, D.; Donnay, G.; Donnay, J.D.H. Jahn–Teller effects in ferro-magnesian minerals: Pyroxenes and olivines. *Bull. Société Fr. Mineral. Cristallogr.* **1974**, *97*, 170–183. [\[CrossRef\]](#)
33. Kullerød, G. *The FeS–ZnS System, a Geological Thermometer*; John, Griegs Boktrykkeri: Bergen, Norway, 1953.
34. Skinner, B.J. Unit-cell edges of natural and synthetic sphalerites. *Am. Mineral. J. Earth Planet. Mater.* **1961**, *46*, 1399–1411.
35. Vallin, J.T.; Slack, G.A.; Roberts, S.; Hughes, A.E. Infrared Absorption in Some II–VI Compounds Doped with Cr. *Phys. Rev. B* **1970**, *2*, 4313–4333. [\[CrossRef\]](#)
36. Nien, Y.-T.; Chen, I.-G. Raman scattering and electroluminescence of ZnS: Cu,Cl phosphor powder. *Appl. Phys. Lett.* **2006**, *89*, 261906. [\[CrossRef\]](#)
37. Sombuthawee, C.; Bonsall, S.B.; Hummel, F.A. Phase equilibria in the systems ZnS–MnS, ZnS–CuInS₂, and MnS–CuInS₂. *J. Solid State Chem.* **1978**, *25*, 391–399. [\[CrossRef\]](#)
38. Kaneko, S.; Aoki, H.; Nonaka, I.; Imoto, F.; Matsumoto, K. Solid Solution and Phase Transformation in the System ZnS–MnS under Hydrothermal Conditions. *J. Electrochem. Soc.* **1983**, *130*, 2487. [\[CrossRef\]](#)
39. Tămaș, C.G.; Andrii, M.P.; Kovács, R.; Drăgușanu, S.; Cauuet, B. Sphalerite Composition in Low- and Intermediate-Sulfidation Epithermal Ore Bodies from the Roșia Montană Au–Ag Ore Deposit, Apuseni Mountains, Romania. *Minerals* **2021**, *11*, 634. [\[CrossRef\]](#)
40. Damian, G.; Buzatu, A.; Apopei, A.I.; Damian, F.; Maftai, A.E. Hydrothermal Sphalerites from Ore Deposits of Baia Mare Area. *Minerals* **2021**, *11*, 1323. [\[CrossRef\]](#)
41. Olivo, G.R.; Gibbs, K. Paragenesis and mineral chemistry of alabandite (MnS) from the Ag-rich Santo Toribio epithermal deposit, Northern Peru. *Mineral. Mag.* **2018**, *67*, 95–102. [\[CrossRef\]](#)
42. Hurai, V.; Huraiová, M. Origin of ferroan alabandite and manganoan sphalerite from the Tisovec skarn, Slovakia. *Neues Jahrb. Mineral. Abh.* **2011**, *188*, 119–134. [\[CrossRef\]](#)
43. Di Benedetto, F. Compositional zoning in sphalerite crystals. *Am. Mineral.* **2005**, *90*, 1384–1392. [\[CrossRef\]](#)
44. Bernardini, G.P.; Borgheresi, M.; Cipriani, C.; Di Benedetto, F.; Romanelli, M. Mn distribution in sphalerite: An EPR study. *Phys. Chem. Miner.* **2004**, *31*, 80–84. [\[CrossRef\]](#)
45. Kelley, K.D. Textural, Compositional, and Sulfur Isotope Variations of Sulfide Minerals in the Red Dog Zn–Pb–Ag Deposits, Brooks Range, Alaska: Implications for Ore Formation. *Econ. Geol.* **2004**, *99*, 1509–1532. [\[CrossRef\]](#)
46. Zhuang, L.; Song, Y.; Liu, Y.; Fard, M.; Hou, Z. Major and trace elements and sulfur isotopes in two stages of sphalerite from the world-class Angouran Zn–Pb deposit, Iran: Implications for mineralization conditions and type. *Ore Geol. Rev.* **2019**, *109*, 184–200. [\[CrossRef\]](#)
47. Gottesmann, W.; Gottesmann, B.S. Sphalerite composition and ore genesis at the Tumurtijn-ovoo Fe–Mn–Zn skarn deposit, Mongolia. *Neues Jahrb. Mineral. Abh.* **2009**, *185*, 249–280. [\[CrossRef\]](#)
48. Wang, L.; Qin, K.-Z.; Song, G.-X.; Li, G.-M. A review of intermediate sulfidation epithermal deposits and subclassification. *Ore Geol. Rev.* **2019**, *107*, 434–456. [\[CrossRef\]](#)
49. Sillitoe, R.H.; Hedenquist, J.W. *Linkages between Volcanotectonic Settings, Ore-Fluid Compositions, and Epithermal Precious Metal Deposits*; Society of Economic Geologists: Littleton, CO, USA, 2005.